

Dynamic winding number for exploring band topology

Bo Zhu,^{1,2} Yongguan Ke,^{1,3} Honghua Zhong,⁴ and Chaohong Lee^{1,2,*}

¹Guangdong Provincial Key Laboratory of Quantum Metrology and Sensing & School of Physics and Astronomy, Sun Yat-Sen University (Zhuhai Campus), Zhuhai 519082, China

²State Key Laboratory of Optoelectronic Materials and Technologies, Sun Yat-Sen University (Guangzhou Campus), Guangzhou 510275, China

³Nonlinear Physics Centre, Research School of Physics, Australian National University, Canberra, Australian Capital Territory 2601, Australia

⁴Institute of Mathematics and Physics, Central South University of Forestry and Technology, Changsha 410004, China



(Received 29 August 2019; revised manuscript received 16 March 2020; accepted 18 March 2020; published 15 April 2020)

Topological invariants play a key role in the characterization of topological states. Because of the existence of exceptional points, it is a great challenge to detect topological invariants in non-Hermitian systems. We put forward a dynamic winding number, the winding of realistic observables in long-time average, for exploring band topology in both Hermitian and non-Hermitian two-band models via a unified approach. We build a concrete relation between dynamic winding numbers and conventional topological invariants. In one dimension, the dynamic winding number directly gives the conventional winding number. In two dimensions, the Chern number is related to the weighted sum of all the dynamic winding numbers of phase singularity points. This work opens a new avenue to measure topological invariants via time-averaged spin textures without requesting any prior knowledge of the system topology.

DOI: [10.1103/PhysRevResearch.2.023043](https://doi.org/10.1103/PhysRevResearch.2.023043)

I. INTRODUCTION

Topological invariant, a global quantity defined with static Bloch functions, has been widely used for classifying and characterizing topological states in various systems, including insulators, superconductors, semimetals, and waveguides [1–6]. Nontrivial topological invariants lead to novel topological effects, such as winding number for quantized geometric phase [7,8], and Chern number for both integer quantum Hall effect [9,10] and the Thouless pumping [11–13]. Measuring topological invariants provides unambiguous evidence for topological states, which apply to precision measurement [14,15], error-resistant spintronics [16,17], and quantum computing [18,19].

Most of the existing methods for measuring topological invariants are mainly based on adiabatic band sweeping [20–24]. However, these methods may fail for imperfect initial states and small energy gaps and become invalid for non-Hermitian systems. Recently, it has been demonstrated that topological invariants can be measured via linking numbers and band-inversion surfaces in quench dynamics [25–30].

However, these quench schemes request prior knowledge of topology before and after quench.

In non-Hermitian systems, due to the emergence of complex spectrum and exceptional points (EPs) [31–33], novel topological states have been theoretically predicted [34–50] and experimentally observed [51–54]. Conventional topological invariants such as winding number and Chern number have been generalized to those in non-Hermitian systems [8,37,55–57], and new topological invariants such as vorticity have also been introduced [58]. Because of the EPs, the winding number may be half of integer in non-Hermitian systems [8,37,59,60]. Besides, non-Bloch definition of Chern number strictly gives the numbers of chiral edge modes [61–64]. The way to measure these topological invariants in non-Hermitian systems is more challenging than that in Hermitian systems. For example, the Hall conductivity is no longer quantized despite being classified as a Chern insulator based on non-Hermitian topological band theory [44,65]. In one dimension, the winding number in a non-Hermitian system has been determined via the mean displacement in long-time quantum walk [66,67], which does not work for measuring Chern numbers and half-integer winding numbers. Is there a unified dynamic approach for measuring topological invariants in both Hermitian and non-Hermitian systems?

In this work, we study a generic two-band model which supports nontrivial topological invariants in both Hermitian and non-Hermitian regions. We define a dynamic winding number (DWN) based on the time-averaged spin textures, which is robust against various initial states. In one dimension, we prove that the DWNs directly give the conventional winding numbers in both chiral-symmetric and

*Corresponding author: lichaoh2@mail.sysu.edu.cn; chleeen@gmail.com

Published by the American Physical Society under the terms of the Creative Commons Attribution 4.0 International license. Further distribution of this work must maintain attribution to the author(s) and the published article's title, journal citation, and DOI.

non-chiral-symmetric systems. In two dimensions, the Chern number is related to the weighted sum of the DWNs around all singularity points (SPs), where the weight is +1 for the north pole and -1 for the south pole. When the system is changed from Hermiticity to non-Hermiticity, each singularity point will be split into two EPs (which are also SPs); yet, the Chern number can still be extracted via the DWNs of all EPs. Without requesting any prior knowledge of their topology, our approach provides general guidance for measuring topological invariants in both Hermitian and non-Hermitian systems.

The paper is organized as follows. In Sec. II, we introduce our physical model and give the definition of DWN. In Sec. III, we consider one-dimensional systems and give the relationship between conventional winding number and DWN. In Sec. IV, we consider two-dimensional systems and give the relationship between Chern number and DWN. In Sec. V, we give a brief conclusion and discussion.

II. DYNAMIC WINDING NUMBER

We consider a general two-band model in d dimension. The Hamiltonian in the momentum space is composed of the three Pauli matrices,

$$H(\mathbf{k}) = h_x(\mathbf{k})\sigma_x + h_y(\mathbf{k})\sigma_y + h_z(\mathbf{k})\sigma_z. \quad (1)$$

Here, \mathbf{k} is the quasimomentum, and $h_{x(y,z)}(\mathbf{k})$ are periodic functions of \mathbf{k} . The Hamiltonian could be Hermitian $H^\dagger(\mathbf{k}) = H(\mathbf{k})$ or non-Hermitian $H^\dagger(\mathbf{k}) \neq H(\mathbf{k})$. Then, the right and left eigenvectors are given by $H(\mathbf{k})|\bar{\varphi}_\mu(\mathbf{k})\rangle = \varepsilon_\mu(\mathbf{k})|\bar{\varphi}_\mu(\mathbf{k})\rangle$ and $H^\dagger(\mathbf{k})|\bar{\chi}_\mu(\mathbf{k})\rangle = \varepsilon_\mu^*(\mathbf{k})|\bar{\chi}_\mu(\mathbf{k})\rangle$, respectively, where $\varepsilon_\mu(\mathbf{k}) = \mu\sqrt{[h_x(\mathbf{k})]^2 + [h_y(\mathbf{k})]^2 + [h_z(\mathbf{k})]^2}$ with $\mu = \pm$ are the eigenvalues. For Hermitian systems, the right and left eigenvectors become the same and hence their corresponding energies, that is, $|\bar{\varphi}_\mu(\mathbf{k})\rangle = |\bar{\chi}_\mu(\mathbf{k})\rangle$ and $\varepsilon_\mu(\mathbf{k}) = \varepsilon_\mu^*(\mathbf{k})$. For non-Hermitian systems, neither the eigenvectors $\{|\bar{\varphi}_\mu(\mathbf{k})\rangle\}$ nor $\{|\bar{\chi}_\mu(\mathbf{k})\rangle\}$ are orthogonal. To account for the nonunitary dynamics of the non-Hermitian systems, we invoke the notion of biorthogonal quantum mechanics [68], and adopt the biorthogonal eigenvectors which fulfill $\langle\chi_\nu(\mathbf{k})|\varphi_\mu(\mathbf{k})\rangle = \delta_{\nu,\mu}$ and $\sum_\mu |\varphi_\mu(\mathbf{k})\rangle\langle\chi_\mu(\mathbf{k})| = 1$ by normalizing $|\varphi_\mu(\mathbf{k})\rangle = |\bar{\varphi}_\mu(\mathbf{k})\rangle/N_\mu(\mathbf{k})$ and $\langle\chi_\mu(\mathbf{k})| = \langle\bar{\chi}_\mu(\mathbf{k})|/N_\mu(\mathbf{k})$ with $N_\mu(\mathbf{k}) = \sqrt{\langle\bar{\chi}_\mu(\mathbf{k})|\bar{\varphi}_\mu(\mathbf{k})\rangle}$.

Considering an arbitrary initial state $|\psi(\mathbf{k}, 0)\rangle = \sum_\mu c_\mu(\mathbf{k})|\varphi_\mu(\mathbf{k})\rangle$ and its associated state $\langle\tilde{\psi}(\mathbf{k}, 0)| = \sum_\mu c_\mu^*(\mathbf{k})\langle\chi_\mu(\mathbf{k})|$, the time evolution of $|\psi(\mathbf{k}, t)\rangle$ and $\langle\tilde{\psi}(\mathbf{k}, t)|$ respectively satisfy

$$\begin{aligned} |\psi(\mathbf{k}, t)\rangle &= \sum_\mu c_\mu(\mathbf{k})e^{-i\varepsilon_\mu(\mathbf{k})t}|\varphi_\mu(\mathbf{k})\rangle, \\ \langle\tilde{\psi}(\mathbf{k}, t)| &= \sum_\mu c_\mu^*(\mathbf{k})e^{i\varepsilon_\mu^*(\mathbf{k})t}\langle\chi_\mu(\mathbf{k})|, \end{aligned} \quad (2)$$

where $c_\mu(\mathbf{k}) = \langle\chi_\mu(\mathbf{k})|\psi(\mathbf{k}, 0)\rangle$. According to the biorthogonal quantum mechanics, the spin textures are given by the expectation values of the Pauli matrices, $\langle\tilde{\psi}(\mathbf{k}, t)|\sigma_j|\psi(\mathbf{k}, t)\rangle$, where $j \in x, y, z$. Here, we are interested in their long-time averages, $\overline{\langle\tilde{\psi}(\mathbf{k}, t)|\sigma_j|\psi(\mathbf{k}, t)\rangle} = \lim_{T \rightarrow \infty} \frac{1}{T} \int_0^T \frac{\langle\tilde{\psi}(\mathbf{k}, t)|\sigma_j|\psi(\mathbf{k}, t)\rangle}{\langle\tilde{\psi}(\mathbf{k}, t)|\psi(\mathbf{k}, t)\rangle} dt$. As the quasimomentum continuously varies, the spin textures of Pauli matrices σ_i and

σ_j will form a trajectory in the polarization plane. The DWN of the spin vectors ($\langle\tilde{\psi}(\mathbf{k}, t)|\sigma_i|\psi(\mathbf{k}, t)\rangle$, $\langle\tilde{\psi}(\mathbf{k}, t)|\sigma_j|\psi(\mathbf{k}, t)\rangle$) is defined as

$$w_d = \frac{1}{2\pi} \oint_S \partial_k \eta_{ji}(\mathbf{k}) \cdot d\mathbf{k}, \quad (3)$$

where S is a closed loop in the parameter space \mathbf{k} , and $\eta_{ji}(\mathbf{k})$ is the dynamical azimuthal angle,

$$\eta_{ji}(\mathbf{k}) = \arctan \left(\frac{\langle\tilde{\psi}(\mathbf{k}, t)|\sigma_j|\psi(\mathbf{k}, t)\rangle}{\langle\tilde{\psi}(\mathbf{k}, t)|\sigma_i|\psi(\mathbf{k}, t)\rangle} \right). \quad (4)$$

On the other hand, we also define the equilibrium azimuthal angle $\phi_{ji}(\mathbf{k})$ in the parameter plane ($h_i(\mathbf{k})$, $h_j(\mathbf{k})$),

$$\phi_{ji}(\mathbf{k}) = \arctan[h_j(\mathbf{k})/h_i(\mathbf{k})]. \quad (5)$$

In the conditions $|c_+(\mathbf{k})|^2 \neq |c_-(\mathbf{k})|^2$ for Hermitian systems and $|c_+(\mathbf{k})|^2 \neq 0 \wedge |c_-(\mathbf{k})|^2 \neq 0$ for non-Hermitian systems, one can easily prove that $\eta_{ji}(\mathbf{k})$ converges to $\phi_{ji}(\mathbf{k})$; see Appendix A. Therefore, in the conditions mentioned above, the DWN can be rewritten as

$$w_d = \frac{1}{2\pi} \oint_S \partial_k \phi_{ji}(\mathbf{k}) \cdot d\mathbf{k}. \quad (6)$$

For Hermitian systems, $|\tilde{\psi}(\mathbf{k}, t)\rangle = |\psi(\mathbf{k}, t)\rangle$, and the dynamical azimuthal angle $\eta_{ji}(\mathbf{k})$ is a real angle, so that the DWN can be directly probed via the long-time average of spin textures $\langle\psi(\mathbf{k}, t)|\sigma_j|\psi(\mathbf{k}, t)\rangle$ in experiment. For non-Hermitian systems, $|\tilde{\psi}(\mathbf{k}, t)\rangle \neq |\psi(\mathbf{k}, t)\rangle$ and $\eta_{ji}(\mathbf{k})$ is a complex angle which cannot be directly observed in experiment. Interestingly, this problem can be fixed by decomposing the azimuthal angle into real and imaginary parts. We find that only the real part of $\eta_{ji}(\mathbf{k})$ contributes to the DWN and it satisfies

$$\begin{aligned} \text{Re}[\eta_{ji}(\mathbf{k})] &= \frac{1}{2} [\phi_{ji}^{RR}(\mathbf{k}) + \phi_{ji}^{LL}(\mathbf{k})] + n\frac{\pi}{2}, \\ \phi_{ji}^{RR}(\mathbf{k}) &= \arctan \left(\frac{\langle\psi(\mathbf{k}, t)|\sigma_j|\psi(\mathbf{k}, t)\rangle}{\langle\psi(\mathbf{k}, t)|\sigma_i|\psi(\mathbf{k}, t)\rangle} \right), \\ \phi_{ji}^{LL}(\mathbf{k}) &= \arctan \left(\frac{\langle\tilde{\psi}(\mathbf{k}, t)|\sigma_j|\tilde{\psi}(\mathbf{k}, t)\rangle}{\langle\tilde{\psi}(\mathbf{k}, t)|\sigma_i|\tilde{\psi}(\mathbf{k}, t)\rangle} \right). \end{aligned} \quad (7)$$

Here, $\text{Re}[\eta_{ji}(\mathbf{k})]$ represents the real part of $\eta_{ji}(\mathbf{k})$, $\phi_{ji}^{RR}(\mathbf{k})$ and $\phi_{ji}^{LL}(\mathbf{k})$ are both real, and n is an integer; see Appendix B. The superscript RR (LL) indicates that the azimuthal angle is calculated in the basis of the right (left) biorthogonal eigenvectors. Thus, we can decompose the DWN as

$$\begin{aligned} w_d &= \frac{1}{2} (w_d^{RR} + w_d^{LL}), \\ w_d^\tau &= \frac{1}{2\pi} \oint_S \partial_k \phi_{ji}^\tau(\mathbf{k}) \cdot d\mathbf{k}, \quad \tau \in RR, LL. \end{aligned} \quad (8)$$

The above results mean that the DWN can also be observed in non-Hermitian systems via the time evolution of the left-left and right-right spin textures whose dynamics are respectively governed by $H(\mathbf{k})$ and $H^\dagger(\mathbf{k})$. In the following sections, we show how to utilize the DWN to uncover the topology in both Hermitian and non-Hermitian systems. For simplicity, we will

use $\overline{\sigma_j}$ and $\widetilde{\sigma_j}$ to denote the long-time average of spin textures $\langle \psi(\mathbf{k}, t) | \sigma_j | \psi(\mathbf{k}, t) \rangle$ and $\langle \tilde{\psi}(\mathbf{k}, t) | \sigma_j | \tilde{\psi}(\mathbf{k}, t) \rangle$, respectively.

III. CONNECTION BETWEEN CONVENTIONAL WINDING NUMBER AND DYNAMIC WINDING NUMBER

In one dimension, if $h_z = 0$, the Hamiltonian (1) has chiral symmetry $\Gamma H \Gamma = -H$ with $\Gamma = i\sigma_x \sigma_y$ and $\mathbf{k} \rightarrow k$.

The conventional winding number w_{\pm} for the Hamiltonian (1) reads

$$\begin{aligned} w_{\pm} &= \frac{1}{2\pi} \oint_S dk \frac{h_x \partial_k h_y - h_y \partial_k h_x}{(\varepsilon_{\pm})^2} \\ &= \frac{1}{2\pi} \oint_S \partial_k \phi_{yx} dk, \end{aligned} \quad (9)$$

which is known as the Zak phase. According to Eqs. (6) and (9), if the initial states satisfy $|c_+(k)|^2 \neq |c_-(k)|^2$ for Hermitian systems and $|c_+(k)|^2 \neq 0 \wedge |c_-(k)|^2 \neq 0$ for non-Hermitian systems, one can find that $w_{\pm} = w_d$.

If $h_z \neq 0$, the Hamiltonian (1) breaks the chiral symmetry. The winding numbers w_{\pm} are given by

$$w_{\pm} = \frac{1}{2\pi} \oint_S dk \frac{h_x \partial_k h_y - h_y \partial_k h_x}{\varepsilon_{\pm}(\varepsilon_{\pm} - h_z)}. \quad (10)$$

Unlike the systems with chiral symmetry, the conventional winding number for each band is not a quantized number, which indicates that w_{\pm} are no longer topological invariants. However, the sum of two conventional winding numbers,

$$\begin{aligned} w_t &= w_+ + w_- = \frac{1}{\pi} \oint_S dk \frac{h_x \partial_k h_y - h_y \partial_k h_x}{h_x^2 + h_y^2} \\ &= \frac{1}{\pi} \oint_S \partial_k \phi_{yx} dk, \end{aligned} \quad (11)$$

has been demonstrated to be a topological invariant, which takes an integer [35,59]. Similarly, if the initial states satisfy $|c_+(k)|^2 \neq |c_-(k)|^2$ for Hermitian systems and $|c_+(k)|^2 \neq 0 \wedge |c_-(k)|^2 \neq 0$ for non-Hermitian systems, The topological invariant w_t is related to the dynamic winding number via $w_t = 2w_d$.

As an example, we consider a system with $h_x = J_0 + J_1 \cos(k)$, $h_y = J_1 \sin(k) - i\delta$, and $h_z = 0$. In the Hermitian case, the parameters are chosen as $\delta = 0$ and $J_1 = 1$. The conventional winding number $w_{\pm} = 1$ for $|J_0| < J_1$, and $w_{\pm} = 0$ for $|J_0| > J_1$. We first calculate the time evolution of spin textures $\langle \psi(k, t) | \sigma_{x(y)} | \psi(k, t) \rangle$ and their long-time averages with $J_0 = 0.5J_1$; see Figs. 1(a)–1(c). The spin textures $\langle \psi(k, t) | \sigma_{x(y)} | \psi(k, t) \rangle$ oscillate with a momentum-dependent period $t_k = \pi/|\varepsilon_{\mu}(k)|$, and their long-time averages $\overline{\sigma_{x(y)}}$ depend on quasimomentum k ; see the black and red lines in Fig. 1(c). With $\overline{\sigma_x}$ and $\overline{\sigma_y}$, we calculate $\eta_{yx}(k)$ as a function of k in Fig. 1(d), where two discontinuous points k_1 and k_2 appear. The DWN can be obtained via the integral of a piecewise function,

$$w_d = \frac{1}{2\pi} \left(\int_{-\pi}^{k_1} \partial_k \eta_{yx} dk + \int_{k_1}^{k_2} \partial_k \eta_{yx} dk + \int_{k_2}^{\pi} \partial_k \eta_{yx} dk \right).$$

We find that the DWN is equal to 1, the same as the conventional winding number w_{\pm} .

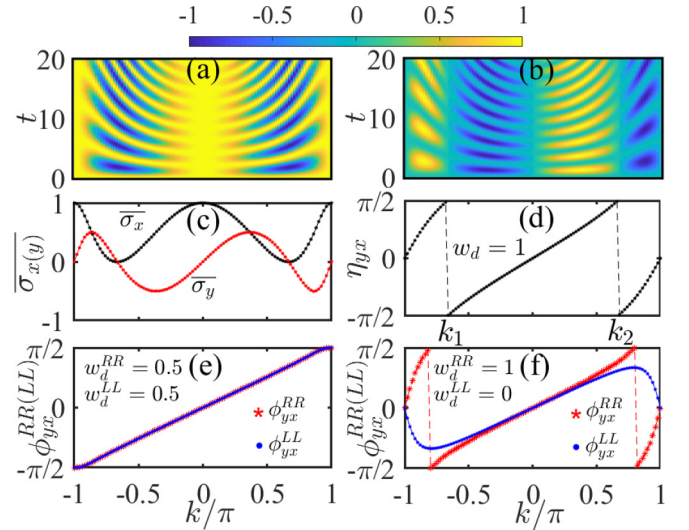


FIG. 1. Extracting conventional winding number via dynamic winding number. Hermitian case ($\delta = 0$): Panels (a) and (b) respectively show the time evolution of the spin textures $\langle \psi(k, t) | \sigma_x | \psi(k, t) \rangle$ and $\langle \psi(k, t) | \sigma_y | \psi(k, t) \rangle$. (c) Long-time average of spin textures $\overline{\sigma_x}$ (black line) and $\overline{\sigma_y}$ (red line) as a function of k , and (d) the dynamical azimuthal angle $\eta_{yx}(k)$ as a function of k , where k_1 and k_2 are discontinuity points. Non-Hermitian case ($\delta = 0.3$): $\phi_{yx}^{RR}(k)$ and $\phi_{yx}^{LL}(k)$ as a function of k for (e) the chiral-symmetric system with $h_z = 0$ and (f) the non-chiral-symmetric system with $h_z = 0.5$. The other parameters are chosen as $J_1 = 1$ and $T = 80$.

When $\delta \neq 0$, the system becomes non-Hermitian and one always needs to measure both $\phi_{ji}^{RR}(k)$ and $\phi_{ji}^{LL}(k)$ to extract the DWN. For a chiral-symmetric system, the two dynamical azimuthal angles satisfy a universal relation $\phi_{ji}^{RR}(k) = \phi_{ji}^{LL}(k)$, which can be easily proven. For the chosen parameters ($J_0 = J_1 = 1$, $\delta = 0.3$, $h_z = 0$, and $w_{\pm} = 1/2$), we have $w_d^{RR} = w_d^{LL} = 1/2$; see Fig. 1(e). It means that we only need to measure $\phi_{ji}^{RR}(k)$ or $\phi_{ji}^{LL}(k)$ in experiments. For a non-chiral-symmetric system (whose parameters are chosen as $J_0 = J_1 = 1$, $\delta = 0.3$, $h_z = 0.5$, and $w_t = 1$), we find $\phi_{ji}^{RR}(k) \neq \phi_{ji}^{LL}(k)$, $w_d^{RR} = 1$, and $w_d^{LL} = 0$; see Fig. 1(f). Nevertheless, the conventional winding number can be obtained by measuring $w_d = (w_d^{RR} + w_d^{LL})/2$ in both chiral and nonchiral symmetric systems.

In Appendix C, we provide more examples about the measurement of conventional winding number in the presence or absence of chiral symmetry. For non-Hermitian systems with chiral symmetry, the winding number for non-Hermitian chiral systems may take value of a half-integer. This is because the winding number is equal to half of the summation of two winding numbers (v_1 and v_2) associated with two EPs, where v_1 and v_2 can only take integers [8].

IV. CONNECTION BETWEEN CHERN NUMBER AND DYNAMIC WINDING NUMBER

By generalizing the concept of gapped band structures from Hermitian to non-Hermitian systems, the Chern number for an energy-separable band can be constructed in a similar way [57]. In contrast to Hermitian systems, there are left-right, right-right, left-left, and right-left Chern

numbers in non-Hermitian systems, depending on the definitions of Berry connection, $A_k^{LR} = i\langle\chi_\mu|\partial_k|\varphi_\mu\rangle$, $A_k^{RR} = i\langle\varphi_\mu|\partial_k|\varphi_\mu\rangle$, $A_k^{LL} = i\langle\chi_\mu|\partial_k|\chi_\mu\rangle$, and $A_k^{RL} = i\langle\varphi_\mu|\partial_k|\chi_\mu\rangle$. Although the corresponding Berry curvatures are locally different quantities, the four kinds of Chern numbers are the same [57]. Here, we only focus on analyzing the Chern number defined with left-right Berry connection $A_k^{LR} = i\langle\chi_\mu|\partial_k|\varphi_\mu\rangle$, which naturally reduces to $i\langle\chi_\mu|\partial_k|\chi_\mu\rangle$ in Hermitian systems.

We map the Hamiltonian to a normalized vector, $\vec{n}(\mathbf{k}) = [\sin(\theta_i)\cos(\phi_{jl}), \sin(\theta_i)\sin(\phi_{jl}), \cos(\theta_i)]$, which reduces to a Bloch vector in Hermitian systems. Here, $\theta_i(\mathbf{k})$ denotes the angle between the vector and the axis i , and $\phi_{jl}(\mathbf{k})$ denotes the equilibrium azimuthal angle in the $j-l$ plane. We can freely choose the reference axis without affecting the validity of the dynamic approach. Then, the left and right eigenvectors for the lower energy band are given by

$$\begin{aligned} \langle\chi_-(\mathbf{k})| &= (-e^{i\phi_{jl}/2}\cos(\frac{\theta_i}{2}), e^{-i\phi_{jl}/2}\sin(\frac{\theta_i}{2})), \\ |\varphi_-(\mathbf{k})\rangle &= \begin{pmatrix} -e^{-i\phi_{jl}/2}\cos(\frac{\theta_i}{2}) \\ e^{i\phi_{jl}/2}\sin(\frac{\theta_i}{2}) \end{pmatrix}. \end{aligned} \quad (12)$$

The right and left eigenstates have phase singularities at $\vec{n}(\mathbf{k}_0) = (0, 0, \pm 1)$, in which $+$ and $-$ respectively correspond to north and south poles. In the parameter space $\mathbf{k} \rightarrow (k_x, k_y)$, the locations \mathbf{k}_0 of the poles satisfy $h_j(\mathbf{k}_0)^2 + h_l(\mathbf{k}_0)^2 = 0$. The left-right Berry connections $A_{k_{x(y)}}^{LR}$ of the lower energy band are given by

$$A_{k_{x(y)}}^{LR} = i\langle\chi_-|\partial_{k_{x(y)}}|\varphi_- \rangle = \frac{\cos(\theta_i)}{2} \frac{\partial\phi_{jl}}{\partial k_{x(y)}}.$$

We discretize the parameter space (k_x, k_y) as $N \times M$ mesh grids in the first Brillouin zone [69,70]. For each grid, a direct application of the two-dimensional Stokes theorem implies that the Chern number reads

$$C = \frac{1}{2\pi} \sum_{l_x=1}^N \sum_{l_y=1}^M \oint_{S_{l_x, l_y}} (A_{k_x}^{LR} dk_x + A_{k_y}^{LR} dk_y), \quad (13)$$

where S_{l_x, l_y} represents the clockwise path integration for the (l_x, l_y) grid. Then, we find that the Chern number is determined by the winding numbers for all SPs, where $\cos[\theta_i(\mathbf{k}_0)] = h_i(\mathbf{k}_0)/|\vec{h}(\mathbf{k}_0)| = \text{sgn}(\text{Re}[h_i(\mathbf{k}_0)]) = 1$ for the north SPs and $\cos[\theta_i(\mathbf{k}_0)] = -1$ for the south SPs, $\text{Re}[h_i(\mathbf{k}_0)]$ represents the real part of $h_i(\mathbf{k}_0)$, and $\vec{h}(\mathbf{k}_0) = [h_x(\mathbf{k}_0), h_y(\mathbf{k}_0), h_z(\mathbf{k}_0)]$. At last, we can deduce the Chern number as

$$C = \frac{1}{2} \sum_{\mathbf{k}_0 \in \text{SPs}} \text{sgn}(\text{Re}[h_i(\mathbf{k}_0)]) w(\mathbf{k}_0), \quad (14)$$

where $w(\mathbf{k}_0) = \frac{1}{2\pi} \oint_{S_{l_x, l_y}} \partial_k \phi_{jl} d\mathbf{k}$ is the winding number for the SP at \mathbf{k}_0 .

Accordingly, if the initial states satisfy $|c_+(\mathbf{k})|^2 \neq |c_-(\mathbf{k})|^2$ for Hermitian systems and $|c_+(\mathbf{k})|^2 \neq 0 \wedge |c_-(\mathbf{k})|^2 \neq 0$ for non-Hermitian systems, one can also find that the DWN $w_d(\mathbf{k}_0) = w(\mathbf{k}_0)$. In the Hermitian case, w_d is related to the dynamical azimuthal angle $\eta_{jl}(\mathbf{k})$, which can be extracted via the right-right spin textures $\langle\psi(\mathbf{k}, t)|\sigma_{j(l)}|\psi(\mathbf{k}, t)\rangle$ due to $|\psi(\mathbf{k}, t)\rangle = |\tilde{\psi}(\mathbf{k}, t)\rangle$. In the non-Hermitian case, w_d is related to the two real dynamical azimuthal angles $\phi_{jl}^{RR}(\mathbf{k})$

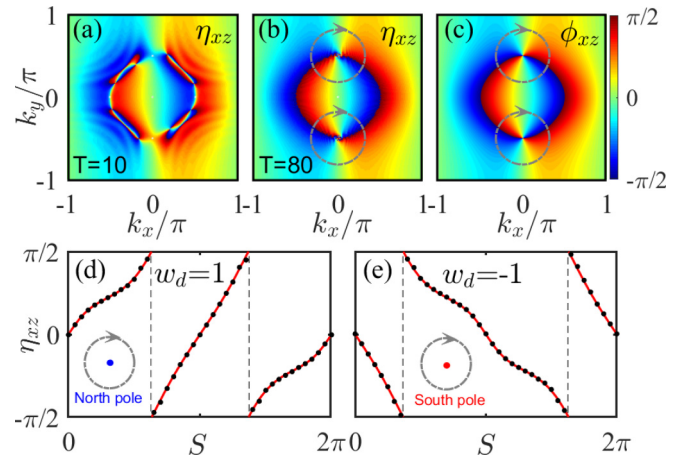


FIG. 2. Topologically nontrivial phase with Chern number $C = 1$. Panels (a) and (b) respectively show dynamical azimuthal angle $\eta_{xz}(\mathbf{k})$ obtained in the evolved time $T = 10$ and $T = 80$, and panel (c) displays equilibrium azimuthal angle $\phi_{xz}(\mathbf{k})$. Panels (d) and (e) show how $\eta_{xz}(\mathbf{k})$ (black dots) and $\phi_{xz}(\mathbf{k})$ (red line) change along the trajectory around the north and south poles in panels (b) and (c), respectively. The other parameters are chosen as $J_{x(y,z)} = 1$, $m_z = 1$, and $\delta = 0$.

and $\phi_{jl}^{LL}(\mathbf{k})$, which can be respectively extracted via right-right spin textures $\langle\psi(\mathbf{k}, t)|\sigma_{j(l)}|\psi(\mathbf{k}, t)\rangle$ and the left-left spin textures $\langle\tilde{\psi}(\mathbf{k}, t)|\sigma_{j(l)}|\tilde{\psi}(\mathbf{k}, t)\rangle$.

As an example, we consider $h_x = J_x \sin(k_x)$, $h_y = J_y \sin(k_y)$, and $h_z = m_z - J_z \cos(k_x) - J_z \cos(k_y) - i\delta$. Here, $J_{x(y,z)}$ denote spin-orbit coupling parameters, m_z is the effective magnetization, and δ is the gain or loss strength. When $\delta = 0$, the system supports quantum anomalous Hall effect [71], which has been realized in recent experiments [27,72]. In the Hermitian case ($J_{x(y,z)} = 1$, $m_z = 1$, $\delta = 0$), the north and south poles in the parameter space (k_x, k_y) can be determined as follows. Since the poles are related to the chosen axis, we select $\theta_y(\mathbf{k}) = \arccos(h_y/|\vec{h}|)$ and $\phi_{xz}(\mathbf{k}) = \arctan(h_x/h_z)$. However, the validity of our dynamic approach is independent of the choice of reference axis; see Appendix D. In the parameter space (k_x, k_y) , by solving $h_x^2 + h_z^2 = 0$, we find that the north and south poles are located at $\mathbf{k}_0 = (k_x, k_y) = (0, \pm\pi/2)$. Then, we need to extract the DWNs around the two poles. We calculate the time evolution of spin textures $\langle\psi(\mathbf{k}, t)|\sigma_x|\psi(\mathbf{k}, t)\rangle$ and $\langle\psi(\mathbf{k}, t)|\sigma_z|\psi(\mathbf{k}, t)\rangle$, and the dynamical azimuthal angle $\eta_{xz}(\mathbf{k})$ can be extracted via long-time average values $\overline{\sigma_{xz}}$; see Figs. 2(a) and 2(b). We also calculate the equilibrium azimuthal angle $\phi_{xz}(\mathbf{k})$ via the eigenstates; see Fig. 2(c). Even in the relatively short time [Fig. 2(a)], the profiles of dynamical azimuthal angle are close to those of the equilibrium azimuthal angle. The difference between $\eta_{xz}(\mathbf{k})$ and $\phi_{xz}(\mathbf{k})$ gradually disappears with the increase of total time T . Thus, we can obtain the DWNs for the north and south poles via integrating the gradient of $\eta_{xz}(\mathbf{k})$ in Figs. 2(d) and 2(e), respectively. The DWNs for the north and south poles are respectively given by $w_d = \pm 1$. Applying Eq. (14), one can obtain the Chern number as 1, which is consistent with the one calculated via integrating the static Berry curvature over the whole Brillouin zone.

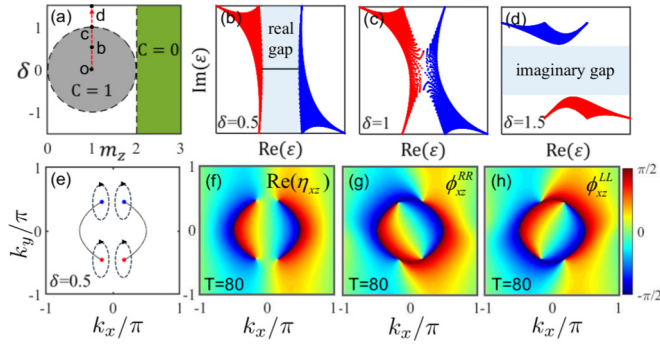


FIG. 3. (a) Topological phase diagram. [(b)–(d)] The bulk bands (red and blue regions) and edge modes (black line) in the complex energy plane, corresponding to the parameter points b – d in panel (a). (e) North EPs (blue dots) and south EPs (red dots) with $J_{x(y,z)} = 1$, $m_z = 1$, and $\delta = 0.5$. [(f)–(h)] Dynamical azimuthal angles $\text{Re}[\eta_{xz}(\mathbf{k})]$, $\phi_{xz}^{RR}(\mathbf{k})$, and $\phi_{xz}^{LL}(\mathbf{k})$, which are defined with left-right, right-right, and left-left spin textures at $T = 80$.

For more general cases, we first show the topological phase diagram in the parameter plane (m_z, δ) by setting $J_{x(y,z)} = 1$; see Fig. 3(a). When the energy bands are separable (i.e., the real parts of energy bands are gapped), the Chern number can be constructed via a method similar to that used in Hermitian systems [57]. In this case, the Chern numbers of the first band are $C = 0$ and 1 in the green and gray regions, respectively. However, the Chern number is not well defined in the white region, because the energy bands are not separable. The boundaries satisfy $(m_z - 1)^2 + \delta^2 < 1$ for the gray region and $m_z > 2$ for the green region. Varying δ along the dashed red arrow, we explore the correspondence between the Chern number and the edge modes under open boundary condition in Figs. 3(b)–3(d), corresponding to the parameter points b – d . For the topologically nontrivial phase, one can see that the complex bulk bands are still gapped and the edge-state modes are still preserved in the real energy axis; see Fig. 3(b). Now we consider $\delta = 0.5$ and keep the other parameters the same as those in Fig. 2(b). We find that the two poles in Hermitian case are split into four EPs if the non-Hermiticity is present; see Fig. 3(e). The blue and red points represent north and south EPs, respectively. In Fig. 3(f), we give $\text{Re}[\eta_{xz}(\mathbf{k})]$ in the parameter space (k_x, k_y) , and the DWNs can be obtained by integrating the gradient of the dynamical azimuthal angle along the trajectory enclosing the north and south EPs. Here, DWNs for the north and south EPs are $w_d = 1/2$ and $-1/2$, respectively. Although the SPs are doubled, as each DWN is reduced by half, the Chern number remains unchanged. For completeness, we also show the dynamical azimuthal angles defined with the right-right and left-left spin textures; see Figs. 3(g) and 3(h). The dynamical azimuthal angles are quite different from each other, corresponding to $\phi_{xz}^{RR}(\mathbf{k})$ and $\phi_{xz}^{LL}(\mathbf{k})$, respectively. Nevertheless, the north and south EPs are the same as those in Fig. 3(e). Around an EP, one can extract the right-right and left-left DWNs w_d^{RR} and w_d^{LL} , which satisfy $w_d = \frac{1}{2}(w_d^{RR} + w_d^{LL})$. One important thing is that $\phi_{xz}^{RR}(\mathbf{k})$ and $\phi_{xz}^{LL}(\mathbf{k})$ defined with the real left-left and right-right spin textures are accessible in experimental measurements.

In addition, our approach can also apply to extract larger Chern number without extra efforts, but it is very hard to access by adiabatic band sweeping; see Appendix D.

V. CONCLUSION AND DISCUSSION

We put forward a new concept of dynamic winding number (DWN) and uncover its connections to conventional topological invariants in both Hermitian and non-Hermitian models. Given a time-averaged spin texture in the parameter space, a DWN is given by a loop integral of the dynamical azimuthal angle gradient enclosing a single singularity point. We find that (i) the conventional winding numbers in one-dimensional systems can be directly given by the corresponding DWNs and (ii) the Chern numbers in two-dimensional systems is related to the weighted sum of all corresponding DWNs. Our scheme has two main advantages. First, in contrast to the quench schemes via measuring linking numbers [25,29] and band-inversion surfaces [27,28], which request prior knowledge of topology before and after a quench, our scheme does not request any prior knowledge. Second, our scheme can be used to measure half-integer winding numbers in one-dimensional non-Hermitian systems, which cannot be measured via previous methods.

Our scheme is readily realized in various systems, ranging from cold atoms in optical lattices, optical waveguide arrays, to optomechanical devices. In Appendix E, we provide more details about the experimental realization of our scheme via cold atoms and optical waveguide arrays. In the future, it would be interesting to extend our scheme to measure topological invariants in high-dimensional systems, multiband systems, periodically driven systems, and disordered systems.

ACKNOWLEDGMENTS

This work is supported by the Key-Area Research and Development Program of Guangdong Province under Grant No. 2019B030330001; the National Natural Science Foundation of China (NNSFC) under Grants No. 11874434, No. 11574405, No. 11805283, and No. 11904419; and the Science and Technology Program of Guangzhou (China) under Grant No. 201904020024. Y.K. is partially supported by the Office of China Postdoctoral Council (Grant No. 20180052), the National Natural Science Foundation of China (Grant No. 11904419), and the Australian Research Council (DP200101168). H.Z. is partially supported by the Hunan Provincial Natural Science Foundation under Grant No. 2019JJ30044. We are deeply grateful to our anonymous reviewers for their thoughtful suggestions that have helped to improve this paper substantially.

B.Z. and Y.K. contributed equally to the work.

APPENDIX A: CONVERGENCE OF DYNAMIC WINDING NUMBER

According to Eq. (2) in the main text, it seems that the definition of DWN depends on the initial state, and it is unclear whether such number converges in the long time. Here, we prove that the initial state can be rather general and the DWN is convergent. The time average of $\langle \tilde{\psi}(\mathbf{k}, t) | \sigma_j | \psi(\mathbf{k}, t) \rangle$

is given by

$$\begin{aligned} & \overline{\langle \tilde{\psi}(\mathbf{k}, t) | \sigma_j | \psi(\mathbf{k}, t) \rangle} \\ &= \lim_{T \rightarrow \infty} \frac{1}{T} \int_0^T \frac{\langle \tilde{\psi}(\mathbf{k}, t) | \sigma_j | \psi(\mathbf{k}, t) \rangle}{\langle \tilde{\psi}(\mathbf{k}, t) | \psi(\mathbf{k}, t) \rangle} dt \\ &= \lim_{T \rightarrow \infty} \frac{1}{T} \int_0^T \frac{\sum_{\mu, \mu'} c_\mu c_{\mu'}^* e^{-i(\varepsilon_\mu - \varepsilon_{\mu'}^*)t} \langle \chi_{\mu'} | \sigma_j | \varphi_\mu \rangle}{\sum_\mu |c_\mu|^2 e^{-i(\varepsilon_\mu - \varepsilon_\mu^*)t}} dt. \end{aligned} \quad (\text{A1})$$

We assume that the eigenenergy $\varepsilon_\mu(\mathbf{k}) = \mu(A + iB)$, $\mu = \pm$, where A and B are \mathbf{k} -dependent real numbers. Then Eq. (A1) can be written as

$$\begin{aligned} & \overline{\langle \tilde{\psi}(\mathbf{k}, t) | \sigma_j | \psi(\mathbf{k}, t) \rangle} \\ &= \lim_{T \rightarrow \infty} \frac{1}{T} \int_0^T \frac{c_- c_-^* e^{-2Bt} \langle \chi_- | \sigma_j | \varphi_- \rangle}{\sum_\mu |c_\mu|^2 e^{-i(\varepsilon_\mu - \varepsilon_\mu^*)t}} dt \\ &+ \lim_{T \rightarrow \infty} \frac{1}{T} \int_0^T \frac{c_+ c_+^* e^{2Bt} \langle \chi_+ | \sigma_j | \varphi_+ \rangle}{\sum_\mu |c_\mu|^2 e^{-i(\varepsilon_\mu - \varepsilon_\mu^*)t}} dt \\ &+ \lim_{T \rightarrow \infty} \frac{1}{T} \int_0^T \frac{c_+ c_-^* e^{-i2At} \langle \chi_- | \sigma_j | \varphi_+ \rangle}{\sum_\mu |c_\mu|^2 e^{-i(\varepsilon_\mu - \varepsilon_\mu^*)t}} dt \\ &+ \lim_{T \rightarrow \infty} \frac{1}{T} \int_0^T \frac{c_- c_+^* e^{i2At} \langle \chi_+ | \sigma_j | \varphi_- \rangle}{\sum_\mu |c_\mu|^2 e^{-i(\varepsilon_\mu - \varepsilon_\mu^*)t}} dt. \end{aligned} \quad (\text{A2})$$

Here, we note that the integrals of the third and fourth terms in Eq. (A2) are periodically oscillating functions of time t . Hence, these terms vanish in the long-time average, leaving only the diagonal terms as

$$\begin{aligned} \overline{\langle \tilde{\psi}(\mathbf{k}, t) | \sigma_j | \psi(\mathbf{k}, t) \rangle} &\cong \lim_{T \rightarrow \infty} \frac{1}{T} \int_0^T \left[\frac{|c_-|^2 e^{-2Bt} \langle \chi_- | \sigma_j | \varphi_- \rangle}{|c_-|^2 e^{-2Bt} + |c_+|^2 e^{2Bt}} \right. \\ &\quad \left. + \frac{|c_+|^2 e^{2Bt} \langle \chi_+ | \sigma_j | \varphi_+ \rangle}{|c_-|^2 e^{-2Bt} + |c_+|^2 e^{2Bt}} \right] dt. \end{aligned} \quad (\text{A3})$$

For Hermitian systems, the energies are purely real, i.e., $\varepsilon_\mu = \varepsilon_\mu^*$ and $B = 0$. The above equation can be simplified as

$$\begin{aligned} \overline{\langle \tilde{\psi}(\mathbf{k}, t) | \sigma_j | \psi(\mathbf{k}, t) \rangle} &\cong \sum_\mu |c_\mu|^2 \langle \chi_\mu | \sigma_j | \varphi_\mu \rangle \\ &= (|c_+|^2 - |c_-|^2) \frac{h_j}{\varepsilon_+}. \end{aligned} \quad (\text{A4})$$

Here, $|c_+|^2 \neq |c_-|^2$; otherwise $\overline{\langle \tilde{\psi}(\mathbf{k}, t) | \sigma_j | \psi(\mathbf{k}, t) \rangle} = 0$ and its relation to the static Hamiltonian is lost.

For non-Hermitian systems, when $B > 0$, Eq. (A3) is approximately given by

$$\overline{\langle \tilde{\psi}(\mathbf{k}, t) | \sigma_j | \psi(\mathbf{k}, t) \rangle} \cong \frac{|c_+|^2}{|c_+|^2} \langle \chi_+ | \sigma_j | \varphi_+ \rangle = \frac{h_j}{\varepsilon_+}. \quad (\text{A5})$$

Here, $|c_+|^2 \neq 0$, because the state will completely decay if the initial state is prepared as $|\varphi_- \rangle$. Similarly, when $B < 0$, Eq. (A3) is approximately given by

$$\overline{\langle \tilde{\psi}(\mathbf{k}, t) | \sigma_j | \psi(\mathbf{k}, t) \rangle} \cong \frac{|c_-|^2}{|c_-|^2} \langle \chi_- | \sigma_j | \varphi_- \rangle = \frac{h_j}{\varepsilon_-}, \quad (\text{A6})$$

with $|c_-|^2 \neq 0$. Combining Eqs. (A4), (A5), and (A6), we have

$$\frac{\overline{\langle \tilde{\psi}(\mathbf{k}, t) | \sigma_j | \psi(\mathbf{k}, t) \rangle}}{\overline{\langle \tilde{\psi}(\mathbf{k}, t) | \psi(\mathbf{k}, t) \rangle}} = \frac{h_j}{h_i}, \quad (\text{A7})$$

On the other hand, the denominator in the left-hand side of Eq. (A7) should be nonzero; that is, the initial states should satisfy $|c_+(\mathbf{k})|^2 \neq |c_-(\mathbf{k})|^2$ for Hermitian systems and $|c_+(\mathbf{k})|^2 \neq 0 \wedge |c_-(\mathbf{k})|^2 \neq 0$ for non-Hermitian systems. According to Eq. (A7), one can obtain

$$\begin{aligned} \eta_{ji}(\mathbf{k}) &= \arctan \left(\frac{\langle \chi_\mu | \sigma_j | \varphi_\mu \rangle}{\langle \chi_\mu | \sigma_i | \varphi_\mu \rangle} \right) = \phi_{ji}(\mathbf{k}), \\ \eta_{ji}(\mathbf{k}) &= \arctan \left(\frac{\overline{\langle \tilde{\psi}(\mathbf{k}, t) | \sigma_j | \psi(\mathbf{k}, t) \rangle}}{\overline{\langle \tilde{\psi}(\mathbf{k}, t) | \sigma_i | \psi(\mathbf{k}, t) \rangle}} \right), \\ \phi_{ji}(\mathbf{k}) &= \arctan(h_j/h_i), \end{aligned} \quad (\text{A8})$$

where $\eta_{ji}(\mathbf{k})$ and $\phi_{ji}(\mathbf{k})$ correspond to the dynamical azimuthal angle and equilibrium azimuthal angle, respectively. It means that the DWN also converges in the long-time limit when the initial state satisfies a few constraints.

APPENDIX B: RELATION BETWEEN DYNAMIC WINDING NUMBER AND TIME-AVERAGED SPIN TEXTURES

For the non-Hermitian case, the azimuthal angles $\eta_{ji}(\mathbf{k})$ and $\phi_{ji}(\mathbf{k})$ are generally complex angles, so that they do not represent physical observables in the biorthogonal system.

This problem can be fixed by decomposing the azimuthal angle into two parts, $\phi_{ji}(\mathbf{k}) = \text{Re}[\phi_{ji}(\mathbf{k})] + \text{Im}[\phi_{ji}(\mathbf{k})]$, where $\text{Re}[\phi_{ji}(\mathbf{k})]$ and $\text{Im}[\phi_{ji}(\mathbf{k})]$ represent the real part and the imaginary part of $\phi_{ji}(\mathbf{k})$. The azimuthal angle satisfies

$$\begin{aligned} e^{i2\phi_{ji}} &= e^{i2\text{Re}(\phi_{ji})} e^{-2\text{Im}(\phi_{ji})} = \frac{1 + i \tan(\phi_{ji})}{1 - i \tan(\phi_{ji})} = \frac{h_i + ih_j}{h_i - ih_j}, \\ e^{-2\text{Im}(\phi_{ji})} &= \left| \frac{h_i + ih_j}{h_i - ih_j} \right|. \end{aligned} \quad (\text{B1})$$

$\text{Re}[\phi_{ji}(\mathbf{k})]$ and $\text{Im}[\phi_{ji}(\mathbf{k})]$ contribute to the argument and amplitude of $e^{i2\phi_{ji}(\mathbf{k})}$, respectively. $\text{Im}[\phi_{ji}(\mathbf{k})]$ is a real, continuous, and periodic function of \mathbf{k} , so that $\oint_S \partial_k \text{Im}(\phi_{ji}) d\mathbf{k} = \oint_S \partial_k \text{Im}(\eta_{ji}) d\mathbf{k} = 0$. It means that only the real part of the azimuthal angle contributes to the DWN,

$$w_d = \frac{1}{2\pi} \oint_S \partial_k \text{Re}(\eta_{ji}) d\mathbf{k} = \frac{1}{2\pi} \oint_S \partial_k \text{Re}(\phi_{ji}) d\mathbf{k}. \quad (\text{B2})$$

Next, we will show that the real part of azimuthal angle is a physical observable. According to Eq. (B1), the real part of azimuthal angle satisfies

$$\tan[2\text{Re}(\phi_{ji})] = \frac{\text{Im}\left(\frac{\mathcal{E}h_i + i\mathcal{E}h_j}{\mathcal{E}h_i - i\mathcal{E}h_j}\right)}{\text{Re}\left(\frac{\mathcal{E}h_i + i\mathcal{E}h_j}{\mathcal{E}h_i - i\mathcal{E}h_j}\right)}, \quad (\text{B3})$$

where \mathcal{E} is a nonzero arbitrary constant. After some algebras, one can rewrite the above relation as

$$\begin{aligned} \tan[2\text{Re}(\phi_{ji})] &= \frac{\tan(\phi_{ji}^{RR}) + \tan(\phi_{ji}^{LL})}{1 - \tan(\phi_{ji}^{RR}) \tan(\phi_{ji}^{LL})} \\ &= \tan(\phi_{ji}^{RR} + \phi_{ji}^{LL}), \end{aligned} \quad (\text{B4})$$

where

$$\begin{aligned}\tan(\phi_{ji}^{RR}) &= \frac{\text{Re}(\mathcal{E}h_j) + \text{Im}(\mathcal{E}h_i)}{\text{Re}(\mathcal{E}h_i) - \text{Im}(\mathcal{E}h_j)}, \\ \tan(\phi_{ji}^{LL}) &= \frac{\text{Re}(\mathcal{E}h_j) - \text{Im}(\mathcal{E}h_i)}{\text{Re}(\mathcal{E}h_i) + \text{Im}(\mathcal{E}h_j)},\end{aligned}\quad (\text{B5})$$

which define two real angles $\phi_{ji}^{RR}(\mathbf{k})$ and $\phi_{ji}^{LL}(\mathbf{k})$, respectively. It is worth noting that the two real angles $\phi_{ji}^{RR}(\mathbf{k})$ and $\phi_{ji}^{LL}(\mathbf{k})$ will be changed by different parameters \mathcal{E} , but $\text{Re}[\phi_{ji}(\mathbf{k})]$ remains the same. The relation between $\text{Re}[\phi_{ji}(\mathbf{k})]$ and $\phi_{ji}^{RR}(\mathbf{k})$, $\phi_{ji}^{LL}(\mathbf{k})$ is given by

$$\text{Re}(\phi_{ji}) = \text{Re}(\eta_{ji}) = \frac{1}{2}(\phi_{ji}^{RR} + \phi_{ji}^{LL}) + n\frac{\pi}{2}, \quad (\text{B6})$$

where n is an integer. It indicates the DWN $w_d = \frac{1}{2}(w_d^{RR} + w_d^{LL})$. Here, $w_d^\tau = \frac{1}{2\pi} \oint_S \partial_k \phi_{ji}^\tau \cdot d\mathbf{k}$, $\tau \in RR, LL$.

Interestingly, the two real angles $\phi_{ji}^{RR}(\mathbf{k})$ and $\phi_{ji}^{LL}(\mathbf{k})$ can be respectively replaced by time-averaged spin textures corresponding to $|\psi(\mathbf{k}, t)\rangle$ and $|\tilde{\psi}(\mathbf{k}, t)\rangle$,

$$\begin{aligned}\phi_{ji}^{RR}(\mathbf{k}) &= \arctan\left(\frac{\langle\psi(\mathbf{k}, t)|\sigma_j|\psi(\mathbf{k}, t)\rangle}{\langle\psi(\mathbf{k}, t)|\sigma_i|\psi(\mathbf{k}, t)\rangle}\right), \\ \phi_{ji}^{LL}(\mathbf{k}) &= \arctan\left(\frac{\langle\tilde{\psi}(\mathbf{k}, t)|\sigma_j|\tilde{\psi}(\mathbf{k}, t)\rangle}{\langle\tilde{\psi}(\mathbf{k}, t)|\sigma_i|\tilde{\psi}(\mathbf{k}, t)\rangle}\right),\end{aligned}\quad (\text{B7})$$

where $\overline{\langle\bullet\rangle} = \lim_{T \rightarrow \infty} \frac{1}{T} \int_0^T \langle\bullet\rangle dt$. Equation (B7) indicates that the two real angles $\phi_{ji}^{RR}(\mathbf{k})$ and $\phi_{ji}^{LL}(\mathbf{k})$ are physical observables. For simplicity, we prove the relation with two real angles, $\phi_{yx}^{RR}(\mathbf{k})$ and $\phi_{yx}^{LL}(\mathbf{k})$ in the case of $B > 0$. The right-right spin textures defined with $|\psi(\mathbf{k}, t)\rangle$ satisfy

$$\frac{\langle\psi(\mathbf{k}, t)|\sigma_y|\psi(\mathbf{k}, t)\rangle}{\langle\psi(\mathbf{k}, t)|\sigma_x|\psi(\mathbf{k}, t)\rangle} = \frac{\langle\varphi_+|\sigma_y|\varphi_+\rangle}{\langle\varphi_+|\sigma_x|\varphi_+\rangle}, \quad (\text{B8})$$

and the left-left spin textures defined with $|\tilde{\psi}(\mathbf{k}, t)\rangle$ satisfy

$$\frac{\langle\tilde{\psi}(\mathbf{k}, t)|\sigma_y|\tilde{\psi}(\mathbf{k}, t)\rangle}{\langle\tilde{\psi}(\mathbf{k}, t)|\sigma_x|\tilde{\psi}(\mathbf{k}, t)\rangle} = \frac{\langle\chi_+|\sigma_y|\chi_+\rangle}{\langle\chi_+|\sigma_x|\chi_+\rangle}. \quad (\text{B9})$$

According to the Hamiltonian (1) in the main text, the right and left biorthogonal eigenvectors are given by

$$\begin{aligned}|\varphi_\mu(\mathbf{k})\rangle &= \frac{1}{\sqrt{2\varepsilon_\mu(\varepsilon_\mu - h_z)}}(h_x - ih_y, \varepsilon_\mu - h_z)^T, \\ \langle\chi_\mu(\mathbf{k})| &= \frac{1}{\sqrt{2\varepsilon_\mu(\varepsilon_\mu - h_z)}}(h_x + ih_y, \varepsilon_\mu - h_z),\end{aligned}\quad (\text{B10})$$

where the superscript \hat{T} is the transposition operation. Combining Eqs. (B8), (B9), and (B10), we can immediately obtain

$$\begin{aligned}\frac{\langle\varphi_+|\sigma_y|\varphi_+\rangle}{\langle\varphi_+|\sigma_x|\varphi_+\rangle} &= \frac{\text{Re}(h_y\mathcal{E}_1) + \text{Im}(h_x\mathcal{E}_1)}{\text{Re}(h_x\mathcal{E}_1) - \text{Im}(h_y\mathcal{E}_1)}, \\ \frac{\langle\chi_+|\sigma_y|\chi_+\rangle}{\langle\chi_+|\sigma_x|\chi_+\rangle} &= \frac{\text{Re}(h_y\mathcal{E}_1) - \text{Im}(h_x\mathcal{E}_1)}{\text{Re}(h_x\mathcal{E}_1) + \text{Im}(h_y\mathcal{E}_1)},\end{aligned}\quad (\text{B11})$$

where $\mathcal{E}_1 = h_z^* + \varepsilon_+^*$. Similarly, one can obtain $\mathcal{E}_1 = h_z^* - \varepsilon_+^*$ for the case of $B < 0$. Combining Eqs. (B5) and (B11), one can easily obtain the relation in Eq. (B7).

APPENDIX C: MEASUREMENT OF CONVENTIONAL WINDING NUMBER IN THE PRESENCE OR ABSENCE OF CHIRAL SYMMETRY

The winding number has been widely used for characterizing the topology of Hermitian systems with chiral symmetry. In one dimension, the winding number can apply to both Hermitian and non-Hermitian systems with or without chiral symmetry. Here, we consider a 1D two-band topological system governed by the Hamiltonian,

$$H(k) = h_x\sigma_x + h_y\sigma_y + h_z\sigma_z. \quad (\text{C1})$$

The conventional winding number for each band is defined as [8,59]

$$\begin{aligned}w_\mu &= \frac{1}{\pi} \oint_S dk \langle\chi_\mu|i\partial_k|\varphi_\mu\rangle \\ &= \frac{1}{2\pi} \oint_S dk \frac{h_x\partial_k h_y - h_y\partial_k h_x}{\varepsilon_\mu(\varepsilon_\mu - h_z)},\end{aligned}\quad (\text{C2})$$

where S is a closed loop with k varying from 0 to 2π , $\mu = \pm$. Next, we will build a relation between the conventional winding number and the DWN in different situations.

When $h_z = 0$, the Hamiltonian (C1) has chiral symmetry $\Gamma H(k)\Gamma = -H(k)$ with $\Gamma = i\sigma_y$. The conventional winding numbers for different bands are the same, which we denote as

$$w_\pm = \frac{1}{2\pi} \oint_S dk \frac{h_x\partial_k h_y - h_y\partial_k h_x}{h_x^2 + h_y^2}. \quad (\text{C3})$$

The expression reduces to that in the Hermitian cases when $|\chi_\mu(k)\rangle = |\varphi_\mu(k)\rangle$. If we define an azimuthal angle as $\phi_{yx}(k) = \arctan(h_y/h_x)$, the above equation is given by

$$w_\pm = \frac{1}{2\pi} \oint_S \partial_k \phi_{yx} dk, \quad (\text{C4})$$

According to Eq. (B2), we can immediately conclude that the conventional winding number is equal to the DWN,

$$w_\pm = w_d, \quad (\text{C5})$$

under a few constraints on the initial state: $|c_+(k)|^2 \neq |c_-(k)|^2$ for Hermitian systems and $|c_+(k)|^2 \neq 0 \wedge |c_-(k)|^2 \neq 0$ for non-Hermitian systems. To numerically verify our theory, we consider the systems with $h_x = J_0 + J_1 \cos(k) + J_2 \cos(2k)$ and $h_y = J_1 \sin(k) + J_2 \sin(2k) - i\delta$. In the non-Hermitian case with $\delta \neq 0$, the conventional winding number w_\pm can appear half of integer in some parameter regions, different from integer value in the Hermitian systems. For simplicity, we take $J_1 = 1$, and J_0, J_2 , and δ are real. The dispersion of this Hamiltonian is

$$\varepsilon_\pm(k) = \pm\sqrt{(J_0 - \delta + e^{-ik} + J_2 e^{-2ik})(J_0 + \delta + e^{ik} + J_2 e^{2ik})}. \quad (\text{C6})$$

The energy is symmetric about zero energy, which is ensured by the chiral symmetry. Since the energy gap must close at phase transition points, we can determine the phase boundaries by the band-crossing condition $\varepsilon_\pm(k) = 0$, which yields $J_0 = \pm\delta + 1 - J_2$ and $J_0 = \pm\delta - 1 - J_2$ for arbitrary J_2 . Particularly, $J_0 = J_2 \pm \delta$ if $|J_2| > 0.5$. Fixing $J_1 = 1$, $J_2 = 1$, and $h_z = 0$ and changing both δ and J_0 , we calculate topological phase diagram distinguished by the conventional

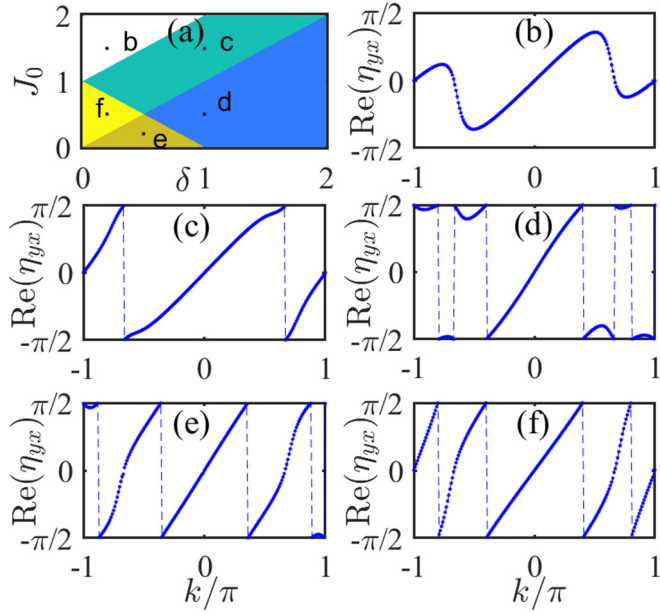


FIG. 4. (a) The phase diagram of the 1D chiral-symmetric topological systems. The white, blue, green, dark-yellow, and bright-yellow regions respectively share winding numbers as $w_{\pm} = 0, 1/2, 1, 3/2$, and 2 . [(b)–(f)] $\text{Re}[\eta_{yx}(k)]$ as a function of k in different parameters (J_0, δ) , which are $(1.5, 0.2)$, $(1.5, 1)$, $(0.5, 1)$, $(0.2, 0.5)$, and $(0.5, 0.2)$, corresponding to points b, c, d, e, and f in panel (a), respectively. The other parameters are chosen as $J_1 = 1$, $J_2 = 1$, and $h_z = 0$.

winding number; see Fig. 4(a). Here, the white, blue, green, dark-yellow, and bright-yellow regions possess conventional winding numbers $w_{\pm} = 0, 1/2, 1, 3/2$, and 2 , respectively. In Figs. 4(b)–4(f), we also give the angle $\text{Re}[\eta_{yx}(k)]$ as a function of the quasimomentum k with different parameters (J_0, δ) marked as b, c, d, e, f in Fig. 4(a).

The DWNs are $0, 1, 1/2, 3/2$, and 2 , respectively. The DWNs extracted from Figs. 4(b)–4(f) are in good agreement with the conventional winding numbers in Fig. 4(a), demonstrating the validity for our dynamic approach once again.

When $h_z \neq 0$, the Hamiltonian (C1) breaks the chiral symmetry. Unlike the systems with chiral symmetry, the conventional winding number for each band is not a quantized number, which indicates that w_{\pm} is no longer a topological invariant. However, the sum of the winding numbers for different bands,

$$w_t = w_+ + w_- = \frac{1}{\pi} \oint_S dk \frac{h_x \partial_k h_y - h_y \partial_k h_x}{h_x^2 + h_y^2}, \quad (\text{C7})$$

has been demonstrated to be a topological invariant [35,59]. The topological invariant w_t is independent of h_z , though its definition is related to the eigenvector of $H(k)$. The parameters h_x and h_y become very important for the definition of topological invariant. Except for the EPs $h_x^2 + h_y^2 = 0$, we introduce a complex angle $\phi_{yx}(k)$ satisfying $\tan[\phi_{yx}(k)] = h_y/h_x$. In term of $\phi_{yx}(k)$, w_t can be represented as

$$w_t = \frac{1}{\pi} \oint_S \partial_k \phi_{yx} dk, \quad (\text{C8})$$

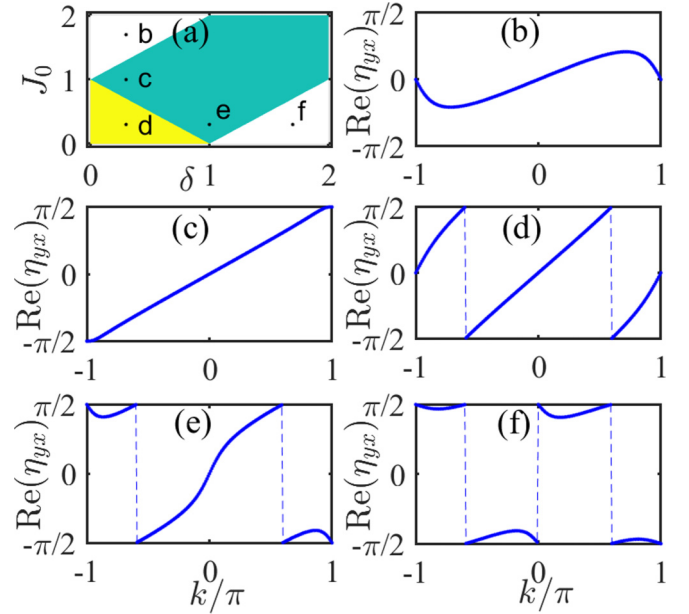


FIG. 5. (a) The phase diagram of the 1D non-chiral-symmetric topological systems. The white, green, and yellow regions share winding number as $w_t = 0, 1$, and 2 , respectively. [(b)–(f)] $\text{Re}[\eta_{yx}(k)]$ as a function of k in different parameters (J_0, δ) , which are $(1.7, 0.3)$, $(1.0, 0.3)$, $(0.3, 0.3)$, $(0.3, 1)$, and $(0.3, 1.7)$, corresponding to points b, c, d, e, and f in panel (a), respectively. The other parameters are chosen as $J_1 = 1$, $J_2 = 0$, and $h_z = 0.5$.

where the integral is also taken along a loop with k varying from 0 to 2π . According to Eq. (B2), we can relate the topological invariant w_t to the DWN

$$w_t = w_+ + w_- = 2w_d, \quad (\text{C9})$$

under a few constraints on the initial state: $|c_+(k)|^2 \neq |c_-(k)|^2$ for Hermitian systems and $|c_+(k)|^2 \neq 0 \wedge |c_-(k)|^2 \neq 0$ for non-Hermitian systems. Fixing $J_1 = 1$, $J_2 = 0$, and $h_z = 0.5$, we calculate the topological invariant w_t as functions of δ and J_0 ; see Fig. 5(a). Here, the white, green, and bright-yellow regions possess topological invariant $w_t = 0, 1$, and 2 , respectively. In Figs. 5(b)–5(f), we also give the angle $\text{Re}[\eta_{yx}(k)]$ versus the quasimomentum k with different parameters (J_0, δ) marked as b, c, d, e, and f in Fig. 5(a).

The DWNs are $0, 1/2, 1, 1/2$, and 0 , respectively. The double of DWNs based on Figs. 5(b)–5(f) are consistent with the equilibrium winding numbers of the phase diagrams in Fig. 5(a), demonstrating the validity of our dynamic approach.

APPENDIX D: ALTERNATE CHOICE OF REFERENCE AXIS AND MEASUREMENT OF LARGER CHERN NUMBER

In the main text, we only consider $\theta_y(\mathbf{k}) = \arccos(h_y/|\vec{h}|)$ and $\phi_{xz}(\mathbf{k}) = \arctan(h_x/h_z)$. Alternatively, we can also take $\theta_z(\mathbf{k}) = \arccos(h_z/|\vec{h}|)$ and $\phi_{yx}(\mathbf{k}) = \arctan(h_y/h_x)$, or $\theta_x(\mathbf{k}) = \arccos(h_x/|\vec{h}|)$ and $\phi_{zy}(\mathbf{k}) = \arctan(h_z/h_y)$. These two choices lead to distinct observations, but give the same Chern number. In Figs. 6(a) and 6(b), based on the different choices of reference axis, we give the azimuthal angle $\phi_{yx}(\mathbf{k})$

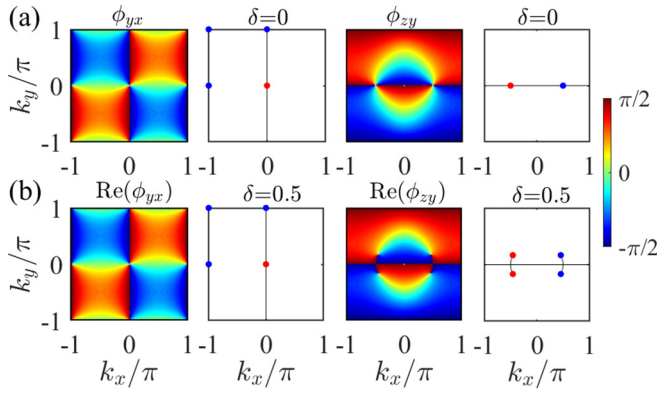


FIG. 6. Topologically nontrivial phase with Chern number $C = 1$. Hermitian case ($\delta = 0$): (a) Azimuthal angle $\phi_{yx}(\mathbf{k})$ and $\phi_{zy}(\mathbf{k})$ in the parameter space $\mathbf{k} \rightarrow (k_x, k_y)$, where blue and red points represent north and south poles of the Bloch spherical surface. Non-Hermitian case ($\delta = 0.5$): (b) Azimuthal angle $\text{Re}[\phi_{yx}(\mathbf{k})]$ and $\text{Re}[\phi_{zy}(\mathbf{k})]$ in the parameter space (k_x, k_y) . Here, blue and red points represent north and south EPs of the virtual Bloch spherical surface. The other parameters are chosen as $J_{x(y,z)} = 1$, $m_z = 1$.

and $\phi_{zy}(\mathbf{k})$ in Hermitian ($\delta = 0$) and non-Hermitian ($\delta = 0.5$) cases, where the other parameters are the same as those in Fig. 2(c) of the main text. Around the singularity points, one can also easily obtain the DWN, and the Chern number $C = 1$ in both the Hermitian and non-Hermitian cases, consistent with the ideal Chern number. This is because these references only differ from a gauge transformation and the Chern number does not depend on the choice of reference.

The dynamic approach is clearly applicable to topological phases with larger Chern numbers. To show this, we consider another two-band model which supports band structure with larger Chern numbers, this is,

$$\begin{aligned} h_x &= J_x \sin(2k_x); h_y = J_y \sin(2k_y); \\ h_z &= m_z - J_z \cos(k_x) - J_z \cos(k_y) - i\delta. \end{aligned} \quad (\text{D1})$$

For the Hermitian case $\delta = 0$, the trivial phase is lying in $|m_z| > 2J_z$, while the topological phases are distinguished as (i) $J_z < m_z < 2J_z$ with the Chern number $C = -1$; (ii) $0 < m_z < J_z$ with $C = 3$; (iii) $-J_z < m_z < 0$ with $C = -3$; and (iv) $-2J_z < m_z < -J_z$ with $C = 1$. Here we only verify topological phase with Chern number $C = 3$, where the other parameters are chosen as $J_x = J_y = 0.2$, $J_z = 1$, and $m_z = 0.5$. In Figs. 7(a) and 7(b), we give the azimuthal angle $\phi_{xz}(\mathbf{k})$ and $\eta_{xz}(\mathbf{k})$ in the parameter space (k_x, k_y) , respectively. One can find that more north and south poles appear in Fig. 7(c), compared with Fig. 2. From Eq. (14), one can also easily obtain the Chern number $C = 3$ via DWN. For the non-Hermitian case, we consider $\delta = 0.1$ and the other parameters are the same as those in the Hermitian case. In Figs. 7(d) and 7(e), we also give the azimuthal angles $\text{Re}[\phi_{xz}(\mathbf{k})]$ and $\text{Re}[\eta_{xz}(\mathbf{k})]$ in the parameter space (k_x, k_y) , respectively. The DWNs around EPs become half, while the EPs become double as the Hermitian counterpart; see Fig. 7(f). Eventually, the Chern number remains the same as that in the Hermitian case.

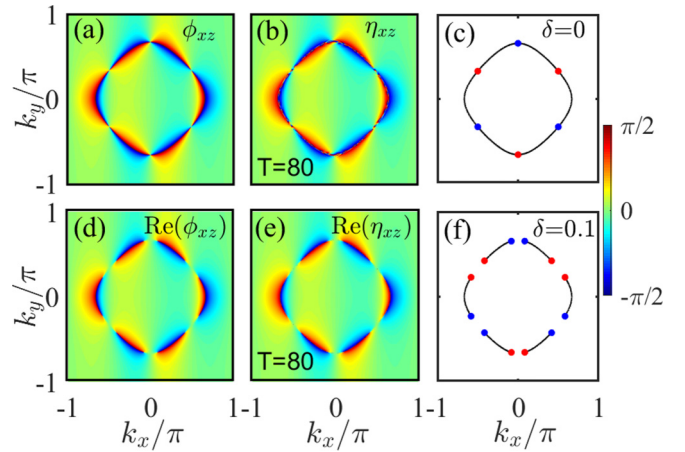


FIG. 7. Topologically nontrivial phase with Chern number $C = 3$. Hermitian case at top ($\delta = 0$): panels (a) and (b) correspond to the azimuthal angle $\phi_{xz}(\mathbf{k})$ and $\eta_{xz}(\mathbf{k})$ in the parameter space $\mathbf{k} \rightarrow (k_x, k_y)$. (c) Blue and red points represent north and south poles of the Bloch spherical surface. Non-Hermitian case at bottom ($\delta = 0.1$): panels (d) and (e) respectively correspond to the azimuthal angle $\text{Re}[\phi_{xz}(\mathbf{k})]$ and $\text{Re}[\eta_{xz}(\mathbf{k})]$ in the parameter space (k_x, k_y) . (f) Blue and red points represent north and south EPs of the virtual Bloch spherical surface. The other parameters are chosen as $J_x = J_y = 0.2$, $J_z = 1$, and $m_z = 0.5$.

APPENDIX E: EXPERIMENTAL CONSIDERATION

One can immediately apply the dynamical approach in topological Hermitian systems. A cold-atom system is an excellent platform to realize topological band models and detect topological invariants. One- and two-dimensional spin-orbit couplings have been realized in a highly controllable Raman lattice [27,73–75]. Initial states are quite easily prepared by loading the atoms into the lattices. Here, the initial constraint $|c_+(\mathbf{k})|^2 \neq |c_-(\mathbf{k})|^2$ may be not satisfied for some specific momentum \mathbf{k} , but the occurrence probability is so small that the global dynamical azimuthal angle is not affected due to the topological nature. The spin population $N_{\uparrow(\downarrow)}(\mathbf{k}, t)$ with different momenta can be measured by spin-resolved time-of-flight (TOF) absorption imaging [27]. Thus, one can obtain the spin population difference $\langle \psi(\mathbf{k}, t) | \sigma_z | \psi(\mathbf{k}, t) \rangle = [N_{\uparrow}(\mathbf{k}, t) - N_{\downarrow}(\mathbf{k}, t)] / [N_{\uparrow}(\mathbf{k}, t) + N_{\downarrow}(\mathbf{k}, t)]$. The spin textures $\langle \psi(\mathbf{k}, t) | \sigma_{x(y)} | \psi(\mathbf{k}, t) \rangle$ can be transferred to the spin population difference by applying $\pi/2$ pulse, that is, $\langle \psi(\mathbf{k}, t) | \sigma_{x(y)} | \psi(\mathbf{k}, t) \rangle = \langle \psi(\mathbf{k}, t) | e^{-i\frac{\pi}{2}\sigma_z} \sigma_{x(y)} e^{i\frac{\pi}{2}\sigma_z} | \psi(\mathbf{k}, t) \rangle$. Because the cold-atom systems have long coherent time, there is no obstacle to extract the DWN via long-time average of the spin textures.

To apply the dynamical approach in topological non-Hermitian systems, we should first consider how to realize the topological non-Hermitian models in experiments. Since two-level non-Hermitian models have been widely realized in optical systems, such as two coupled optical cavities [76,77], optical waveguides [67,78,79], and optomechanical cavity [52,80,81], we mainly discuss how to extract DWN with two optical waveguides with tunable parameters. A two-level non-Hermitian system can be realized by introducing gain and loss

in the two waveguides. The coupling strength can be tuned by the waveguide separation. We regard the two different waveguides as two spin components. The initial states can be prepared by randomly splitting the light injecting into the two waveguides. One can obtain $\langle \psi(\mathbf{k}, l) | \sigma_z | \psi(\mathbf{k}, l) \rangle$ by measuring the intensity difference between two waveguides at propagating distance l . Here, the distance l plays the role of time. Actually, the final states will collapse onto one of

the eigenstates in the long distance. Thus, the output intensity difference of the waveguides is sufficient, and long-distance average of the intensity difference is not necessary. One can also obtain $\langle \psi(\mathbf{k}, l) | \sigma_{x(y)} | \psi(\mathbf{k}, l) \rangle$ by insetting a beam splitter before intensity measurement. By designing the waveguide separation and the gain (loss) rates, one can simulate the two-band model. Repeating the above operations, one can finally construct the DWN.

-
- [1] X. L. Qi and S. C. Zhang, Topological insulators and superconductors, *Rev. Mod. Phys.* **83**, 1057 (2011).
 - [2] B. A. Bernevig and T. L. Hughes, *Topological Insulators and Topological Superconductors* (Princeton University Press, Princeton, NJ, 2013).
 - [3] Y. Ando, Topological insulator materials, *J. Phys. Soc. Jpn.* **82**, 102001 (2013).
 - [4] C. K. Chiu, J. C. Y. Teo, A. P. Schnyder, and S. Ryu, Classification of topological quantum matter with symmetries, *Rev. Mod. Phys.* **88**, 035005 (2016).
 - [5] B. Q. Lv, Z.-L. Feng, Q.-N. Xu, X. Gao, J.-Z. Ma, L.-Y. Kong, P. Richard, Y.-B. Huang, V. N. Strocov, C. Fang *et al.*, Observation of three-component fermions in the topological semimetal molybdenum phosphide, *Nature (London)* **546**, 627 (2017).
 - [6] T. Ozawa, H. M. Price, A. Amo, N. Goldman, M. Hafezi, L. Lu, M. C. Rechtsman, D. Schuster, J. Simon, O. Zilberberg *et al.*, Topological photonics, *Rev. Mod. Phys.* **91**, 015006 (2019).
 - [7] T. Cao, M. Wu, and S. G. Louie, Unifying Optical Selection Rules for Excitons in Two Dimensions: Band Topology and Winding Numbers, *Phys. Rev. Lett.* **120**, 087402 (2018).
 - [8] C. Yin, H. Jiang, L. Li, R. Lü, and S. Chen, Geometrical meaning of winding number and its characterization of topological phases in one-dimensional chiral non-Hermitian systems, *Phys. Rev. A* **97**, 052115 (2018).
 - [9] D. J. Thouless, M. Kohmoto, M. P. Nightingale, and M. den Nijs, Quantized Hall Conductance in a Two-Dimensional Periodic Potential, *Phys. Rev. Lett.* **49**, 405 (1982).
 - [10] Y. Hatsugai, Chern Number and Edge States in the Integer Quantum Hall Effect, *Phys. Rev. Lett.* **71**, 3697 (1993).
 - [11] D. J. Thouless, Quantization of particle transport, *Phys. Rev. B* **27**, 6083 (1983).
 - [12] Y. G. Ke, X. Z. Qin, F. Mei, H. H. Zhong, Y. S. Kivshar, and C. H. Lee, Topological phase transitions and Thouless pumping of light in photonic waveguide arrays, *Laser Photon. Rev.* **10**, 995 (2016).
 - [13] M. Lohse, C. Schweizer, H. M. Price, O. Zilberberg, and I. Bloch, Exploring 4d quantum Hall physics with a 2d topological charge pump, *Nature (London)* **553**, 55 (2018).
 - [14] K. v. Klitzing, G. Dorda, and M. Pepper, New Method for High-Accuracy Determination of the Fine-Structure Constant Based on Quantized Hall Resistance, *Phys. Rev. Lett.* **45**, 494 (1980).
 - [15] N. R. Cooper and A. M. Rey, Adiabatic control of atomic dressed states for transport and sensing, *Phys. Rev. A* **92**, 021401(R) (2015).
 - [16] C. Nayak, S. H. Simon, A. Stern, M. Freedman, and S. Das Sarma, Non-Abelian anyons and topological quantum computation, *Rev. Mod. Phys.* **80**, 1083 (2008).
 - [17] D. Pesin and A. H. MacDonald, Spintronics and pseudospintronics in graphene and topological insulators, *Nat. Mater.* **11**, 409 (2012).
 - [18] F. D. M. Haldane, Nobel lecture: Topological quantum matter, *Rev. Mod. Phys.* **89**, 040502 (2017).
 - [19] B. Lian, X.-Q. Sun, A. Vaezi, X.-L. Qi, and S.-C. Zhang, Topological quantum computation based on chiral majorana fermions, *Proc. Natl. Acad. Sci. U.S.A.* **115**, 10938 (2018).
 - [20] M. Atala, M. Aidelsburger, J. T. Barreiro, D. Abanin, T. Kitagawa, E. Demler, and I. Bloch, Direct measurement of the Zak phase in topological Bloch bands, *Nat. Phys.* **9**, 795 (2013).
 - [21] G. Jotzu, M. Messer, R. Desbuquois, M. Lebrat, T. Uehlinger, D. Greif, and T. Esslinger, Experimental realization of the topological Haldane model with ultracold fermions, *Nature (London)* **515**, 237 (2014).
 - [22] M. Aidelsburger, M. Lohse, C. Schweizer, M. Atala, J. T. Barreiro, S. Nascimbene, N. R. Cooper, I. Bloch, and N. Goldman, Measuring the Chern number of Hofstadter bands with ultracold bosonic atoms, *Nat. Phys.* **11**, 162 (2015).
 - [23] N. Fläschner, B. S. Rem, M. Tarnowski, D. Vogel, D. S. Lühmann, K. Sengstock, and C. Weitenberg, Experimental reconstruction of the Berry curvature in a Floquet Bloch band, *Science* **352**, 1091 (2016).
 - [24] S. Hu, Y. G. Ke, Y. G. Deng, and C. H. Lee, Dispersion-suppressed topological Thouless pumping, *Phys. Rev. B* **100**, 064302 (2019).
 - [25] C. Wang, P. Zhang, X. Chen, J. Yu, and H. Zhai, Scheme to Measure the Topological Number of a Chern Insulator from Quench Dynamics, *Phys. Rev. Lett.* **118**, 185701 (2017).
 - [26] X. Qiu, T. S. Deng, Y. Hu, P. Xue, and W. Yi, Fixed points and emergent topological phenomena in a parity-time-symmetric quantum quench, *iScience* **20**, 392 (2019).
 - [27] W. Sun, C. R. Yi, B. Z. Wang, W. W. Zhang, B. C. Sanders, X. T. Xu, Z. Y. Wang, J. Schmiedmayer, Y. Deng, X. J. Liu *et al.*, Uncover Topology by Quantum Quench Dynamics, *Phys. Rev. Lett.* **121**, 250403 (2018).
 - [28] L. Zhang, L. Zhang, S. Niu, and X.-J. Liu, Dynamical classification of topological quantum phases, *Sci. Bull.* **63**, 1385 (2018).
 - [29] M. Tarnowski, F. N. Ünal, N. Fläschner, B. S. Rem, A. Eckardt, K. Sengstock, and C. Weitenberg, Measuring topology from dynamics by obtaining the Chern number from a linking number, *Nat. Commun.* **10**, 1728 (2019).
 - [30] L. Zhang, L. Zhang, and X. J. Liu, Dynamical detection of topological charges, *Phys. Rev. A* **99**, 053606 (2019).
 - [31] W. D. Heiss, The physics of exceptional points, *J. Phys. A: Math. Theor.* **45**, 444016 (2012).

- [32] W. Hu, H. Wang, P. P. Shum, and Y. D. Chong, Exceptional points in a non-Hermitian topological pump, *Phys. Rev. B* **95**, 184306 (2017).
- [33] A. U. Hassan, B. Zhen, M. Soljačić, M. Khajavikhan, and D. N. Christodoulides, Dynamically Encircling Exceptional Points: Exact Evolution and Polarization State Conversion, *Phys. Rev. Lett.* **118**, 093002 (2017).
- [34] K. Esaki, M. Sato, K. Hasebe, and M. Kohmoto, Edge states and topological phases in non-Hermitian systems, *Phys. Rev. B* **84**, 205128 (2011).
- [35] S.-D. Liang and G.-Y. Huang, Topological invariance and global Berry phase in non-Hermitian systems, *Phys. Rev. A* **87**, 012118 (2013).
- [36] S. Malzard, C. Poli, and H. Schomerus, Topologically Protected Defect States in Open Photonic Systems with Non-Hermitian Charge-Conjugation and Parity-Time Symmetry, *Phys. Rev. Lett.* **115**, 200402 (2015).
- [37] T. E. Lee, Anomalous Edge State in a Non-Hermitian Lattice, *Phys. Rev. Lett.* **116**, 133903 (2016).
- [38] D. Leykam, K. Y. Bliokh, C. Huang, Y. D. Chong, and F. Nori, Edge Modes, Degeneracies, and Topological Numbers in Non-Hermitian Systems, *Phys. Rev. Lett.* **118**, 040401 (2017).
- [39] T. Rakovszky, J. K. Asbóth, and A. Alberti, Detecting topological invariants in chiral symmetric insulators via losses, *Phys. Rev. B* **95**, 201407(R) (2017).
- [40] S. Lieu, Topological phases in the non-Hermitian Su-Schrieffer-Heeger model, *Phys. Rev. B* **97**, 045106 (2018).
- [41] V. M. Martinez Alvarez, J. E. Barrios Vargas, and L. E. F. Foa Torres, Non-Hermitian robust edge states in one dimension: Anomalous localization and eigenspace condensation at exceptional points, *Phys. Rev. B* **97**, 121401(R) (2018).
- [42] T. Yoshida, R. Peters, and N. Kawakami, Non-Hermitian perspective of the band structure in heavy-fermion systems, *Phys. Rev. B* **98**, 035141 (2018).
- [43] L. Zhou and J. B. Gong, Non-Hermitian Floquet topological phases with arbitrarily many real-quasienergy edge states, *Phys. Rev. B* **98**, 205417 (2018).
- [44] Y. Chen and H. Zhai, Hall conductance of a non-Hermitian Chern insulator, *Phys. Rev. B* **98**, 245130 (2018).
- [45] Z. Gong, Y. Ashida, K. Kawabata, K. Takasan, S. Higashikawa, and M. Ueda, Topological phases of non-Hermitian systems, *Phys. Rev. X* **8**, 031079 (2018).
- [46] T. Yoshida, R. Peters, N. Kawakami, and Y. Hatsugai, Symmetry-protected exceptional rings in two-dimensional correlated systems with chiral symmetry, *Phys. Rev. B* **99**, 121101(R) (2019).
- [47] D. S. Borgnia, A. J. Kruchkov, and R. Slager, Non-Hermitian Boundary Modes, *Phys. Rev. Lett.* **124**, 056802 (2020).
- [48] T. Yoshida, K. Kudo, and Y. Hatsugai, Non-Hermitian fractional quantum Hall states, *Sci. Rep.* **9**, 16895 (2019).
- [49] K. Kawabata, K. Shiozaki, M. Ueda, and M. Sato, Symmetry and topology in non-Hermitian physics, *Phys. Rev. X* **9**, 041015 (2019).
- [50] H. Zhou and J. Y. Lee, Periodic table for topological bands with non-Hermitian symmetries, *Phys. Rev. B* **99**, 235112 (2019).
- [51] J. Doppler, A. A. Mailybaev, J. Böhm, U. Kuhl, A. Girschik, F. Libisch, T. J. Milburn, P. Rabl, N. Moiseyev, and S. Rotter, Dynamically encircling an exceptional point for asymmetric mode switching, *Nature (London)* **537**, 76 (2016).
- [52] H. Xu, D. Mason, L. Jiang, and J. G. E. Harris, Topological energy transfer in an optomechanical system with exceptional points, *Nature (London)* **537**, 80 (2016).
- [53] H. Y. Zhou, C. Peng, Y. Yoon, C. W. Hsu, K. A. Nelson, L. Fu, J. D. Joannopoulos, M. Soljačić, and B. Zhen, Observation of bulk Fermi arc and polarization half charge from paired exceptional points, *Science* **359**, 1009 (2018).
- [54] A. Cerjan, S. Huang, M. Wang, K. P. Chen, Y. Chong, and M. C. Rechtsman, Experimental realization of a Weyl exceptional ring, *Nat. Photon.* **13**, 623 (2019).
- [55] Y. Xu, S. T. Wang, and L. M. Duan, Weyl Exceptional Rings in a Three-Dimensional Dissipative Cold Atomic Gas, *Phys. Rev. Lett.* **118**, 045701 (2017).
- [56] A. Cerjan, M. Xiao, L. Yuan, and S. H. Fan, Effects of non-Hermitian perturbations on Weyl Hamiltonians with arbitrary topological charges, *Phys. Rev. B* **97**, 075128 (2018).
- [57] H. Shen, B. Zhen, and L. Fu, Topological Band Theory for Non-Hermitian Hamiltonians, *Phys. Rev. Lett.* **120**, 146402 (2018).
- [58] A. Ghatak and T. Das, New topological invariants in non-Hermitian systems, *J. Phys.: Condens. Matter* **31**, 263001 (2019).
- [59] H. Jiang, C. Yang, and S. Chen, Topological invariants and phase diagrams for one-dimensional two-band non-Hermitian systems without chiral symmetry, *Phys. Rev. A* **98**, 052116 (2018).
- [60] L. Jin and Z. Song, Bulk-boundary correspondence in a non-Hermitian system in one dimension with chiral inversion symmetry, *Phys. Rev. B* **99**, 081103(R) (2019).
- [61] S. Yao and Z. Wang, Edge States and Topological Invariants of Non-Hermitian Systems, *Phys. Rev. Lett.* **121**, 086803 (2018).
- [62] S. Yao, F. Song, and Z. Wang, Non-Hermitian Chern Bands, *Phys. Rev. Lett.* **121**, 136802 (2018).
- [63] A. Ghatak, M. Brandenbourger, J. V. Wezel, and C. Coullais, Observation of non-Hermitian topology and its bulk-edge correspondence, *arXiv:1907.11619*.
- [64] K. Yokomizo and S. Murakami, Non-Bloch Band Theory of Non-Hermitian Systems, *Phys. Rev. Lett.* **123**, 066404 (2019).
- [65] T. M. Philip, M. R. Hirsbrunner, and M. J. Gilbert, Loss of Hall conductivity quantization in a non-Hermitian quantum anomalous Hall insulator, *Phys. Rev. B* **98**, 155430 (2018).
- [66] M. S. Rudner and L. S. Levitov, Topological Transition in a Non-Hermitian Quantum Walk, *Phys. Rev. Lett.* **102**, 065703 (2009).
- [67] J. M. Zeuner, M. C. Rechtsman, Y. Plotnik, Y. Lumer, S. Nolte, M. S. Rudner, M. Segev, and A. Szameit, Observation of a Topological Transition in the Bulk of a Non-Hermitian System, *Phys. Rev. Lett.* **115**, 040402 (2015).
- [68] D. C. Brody, Biorthogonal quantum mechanics, *J. Phys. A: Math. Theor.* **47**, 035305 (2013).
- [69] T. Fukui, Y. Hatsugai, and H. Suzuki, Chern numbers in discretized Brillouin zone: Efficient method of computing (spin) Hall conductances, *J. Phys. Soc. Jpn.* **74**, 1674 (2005).
- [70] J. K. Asbóth, L. Oroszlány, and A. Pályi, A short course on topological insulators, *Lect. Notes Phys.* **919** (2016).
- [71] X. J. Liu, K. T. Law, and T. K. Ng, Realization of 2D Spin-Orbit Interaction and Exotic Topological Orders in Cold Atoms, *Phys. Rev. Lett.* **112**, 086401 (2014).

- [72] C. Z. Chang, J. Zhang, X. Feng, J. Shen, Z. Zhang, M. Guo, K. Li, Y. Ou, P. Wei, L. L. Wang *et al.*, Experimental observation of the quantum anomalous Hall effect in a magnetic topological insulator, *Science* **340**, 167 (2013).
- [73] C. Qu, C. Hamner, M. Gong, C. Zhang, and P. Engels, Observation of *Zitterbewegung* in a spin-orbit-coupled Bose-Einstein condensate, *Phys. Rev. A* **88**, 021604(R) (2013).
- [74] C. Hamner, C. Qu, Y. Zhang, J. Chang, M. Gong, C. Zhang, and P. Engels, Dicke-type phase transition in a spin-orbit-coupled Bose-Einstein condensate, *Nat. Commun.* **5**, 4023 (2014).
- [75] W. Sun, B. Z. Wang, X. T. Xu, C. R. Yi, L. Zhang, Z. Wu, Y. Deng, X. J. Liu, S. Chen, and J. W. Pan, Highly Controllable and Robust 2D Spin-Orbit Coupling for Quantum Gases, *Phys. Rev. Lett.* **121**, 150401 (2018).
- [76] L. Chang, X. Jiang, S. Hua, C. Yang, J. Wen, L. Jiang, G. Li, G. Wang, and M. Xiao, Parity-time symmetry and variable optical isolation in active-passive-coupled microresonators, *Nat. Photon.* **8**, 524 (2014).
- [77] B. Peng, Ş. K. Özdemir, F. Lei, F. Monifi, M. Gianfreda, G. L. Long, S. Fan, F. Nori, C. M. Bender, and L. Yang, Parity-time-symmetric whispering-gallery microcavities, *Nat. Phys.* **10**, 394 (2014).
- [78] J. P. Gordon and H. Kogelnik, PMD fundamentals: Polarization mode dispersion in optical fibers, *Proc. Natl. Acad. Sci. USA* **97**, 4541 (2000).
- [79] C. E. Rüter, K. G. Makris, R. El-Ganainy, D. N. Christodoulides, M. Segev, and D. Kip, Observation of parity-time symmetry in optics, *Nat. Phys.* **6**, 192 (2010).
- [80] M. Aspelmeyer, T. J. Kippenberg, and F. Marquardt, Cavity optomechanics, *Rev. Mod. Phys.* **86**, 1391 (2014).
- [81] E. Verhagen and A. Alù, Optomechanical nonreciprocity, *Nat. Phys.* **13**, 922 (2017).